CHEMIJA. 2020. Vol. 31. No. 3. P. 119–129

Early stages of Mg–Nb alloy corrosion in a balanced salt solution – STEM-HAADF and EIS study

Konstantinas Leinartas,

Eimutis Juzeliūnas*,

Laurynas Staišiūnas,

Algirdas Selskis,

Asta Grigucevičienė,

Dalia Bučinskienė,

Remigijus Juškėnas,

Alma Ručinskienė

Department of Electrochemical Materials Science, Centre for Physical Sciences and Technology, 3 Saulėtekio Avenue, Vilnius, Lithuania

Thin Mg–Nb alloy films having a thickness below 1 μm were deposited by magnetron sputtering on glass substrates with Nb concentrations of 4, 26 and 32 at.%. Distribution of the elements within the deposits was identified by a scanning transmission electron microscope (STEM) equipped with a high angle annular dark field (HAADF) detector, which showed on a nanometer scale fine Nb-enriched structures. XRD identified nano-crystallinity of the deposits with grain sizes of the order of tens of nanometers. The corrosion behaviour of the films has been studied in a balanced salt solution, whose pH and ion concentrations were close to those of the human blood plasma. The electrochemical impedance spectroscopy implied a localized corrosion with diffusion limitations within a layer of corrosion products. The corrosion rates were determined in situ by Tafel extrapolation and EIS-derived polarization resistance; both methods provided reliable results for corrosion resistant alloy with ca. one third of Nb. Alloying of Mg with Nb makes it possible to adjust the corrosion activity of the alloy according to biomedical requirements for in vivo applications.

Keywords: magnesium, niobium, alloy, corrosion, balanced salt solution

INTRODUCTION

While susceptibility of magnesium to corrosion is an issue in many technical fields, this property could be regarded as a valuable one in biomedical applications. Corrosion activity of Mg-based temporary implants, such as cardiovascular stents or tissue scaffolds, enables their dissolution in vivo avoiding secondary surgery for removal [1–10]. Magnesium ions are common in the human body; their cytotoxic activity when released from a metallic state was not determined [11]. The corrosion rate, however, of an implant has to be tailored according to biomedical requirements. The implant degradation during 12–24 months could be reasonable [2, 12]. An opportunity for such tailoring of the degradation rate provides Mg alloying with corrosion resistant and physiologically inert alloying components. Niobium is a potential candidate because it is not toxic and physiologically inert, and also forms a bonelike oxide layer that promotes osteointegration [13, 14].

Alloying of refractory Nb with lightweight Mg is complicated as the melting point of Nb ($T_{m,\ Nb}$ = 2477°C) exceeds by far the boiling point of Mg ($T_{b,\ Mg}$ = 1091°C). Also, Nb and Mg do not form intermetallic phases [15, 16]. Non-thermal

* Corresponding author. Email: eimutis.juzeliunas@ftmc.lt

processes, such as high-energy ball milling or reactive milling in H_2 atmosphere, have been used to produce Mg–Nb alloys [17, 18].

An alloying opportunity provides physical vapour deposition (PVD), which makes it possible to co-deposit Mg with another metal. Thin film compositions can be obtained by PVD, which are of interest for protective purposes of magnesium as well as such subjects as cardiovascular stents, optically switchable mirrors [19, 20] or hydrogen storage devices [21–25]. We deposited thin films of Mg–Nb alloys by co-sputtering of individual targets of both components. It is common knowledge that sputtering techniques make it possible to deposit homogeneous alloy systems. We demonstrate, however, a nano-inhomogeneity of Nb distribution within Mg–Nb structures, which may cause nano-scale galvanic corrosion effects.

Our research aims to study Mg–Nb corrosion at very early stages in a balanced salt solution, whose pH and ion concentrations were close to those of the human blood plasma. The initial corrosion attracted a considerable attention due to a possibility to better understand the corrosion behaviour in a long run. Early stage corrosion of numerous metals has recently been investigated: tin [26], uranium [27], aluminium [28], magnesium and copper [29]. Corrosion of alloys has also been investigated at initial stages: steel [30–36], nickel and cobalt superalloys [37], copper–tin bronze [38] as well as zirconium [39], magnesium [40] and aluminum alloys [41, 42]. The authors proposed various innovative approaches such as colorimetric indicators [26], strain gauges [30], electrochemical atomic force microscopy [33, 34], fiber grating sensor [36], QCN sensors with glued foil electrodes [28], polymer coatings with fluorescence indicators [29], in situ FTIR and Raman spectroscopy [38, 39], ultramicrotomy [41], optical probe based on plasmonic nanoparticles [42], radiofrequency wave propagation [43] and electrical resistance sensors [44].

Here we show the interface study of Mg–Nb systems at early corrosion stages performed using both ex situ and in situ techniques. To that end, a scanning transmission electron microscope (STEM) in conjunction with a high angle annular dark field (HAADF) detector has been used for ex situ investigations and the electrochemical impedance spectroscopy (EIS) was applied as an in situ non-destructive technique.

EXPERIMENTAL

Magnetron sputtering of Mg and Nb targets was performed using a Univex 350 vacuum system from Leybold Vacuum GmbH equipped with two confocal DC magnetrons. The sputtering chamber was evacuated up to 2.2×10^{-6} mbar and then filled with a working gas (Ar), maintaining the gas pressure at 1.6×10^{-3} mbar. The targets were prepared from pure Mg (99.9%) and Nb (99.9%) both from Alfa Aesar GmbH. Glass discs of 14 mm in diameter were used as substrates, which were kept at 60°C by an integrated infrared heater during the deposition. The sputtering power was from 95 to 110 W for Mg and from 5 to 90 W for Nb. A holder with the substrates was rotated at a frequency of 13 rpm to ensure a uniform coating distribution. The magnesium/niobium ratio (c_{Mg}/c_{Nb}) in the deposits was changed by varying the sputtering power of the magnetrons. The thickness of the Mg-*x*Nb alloys films was ca. 600 to 800 nm. The prepared samples were kept in a chamber filled with N_2 gas under ambient conditions.

Crystallographic structures were studied by X-ray diffraction (XRD) using a D8 Advance diffractometer (Bruker AXS) equipped with a Goebel mirror – a primary beam monochromator for CuKα radiation. A step scan mode was used in the 2θ range from 30 to 75° with a step length of 0.02° and a counting time of 5 s per step.

The morphology and composition of the deposits were examined by SEM Helios NanoLab 650 (FEI) equipped with an energy dispersive X-ray spectrometer (EDX) INCAEnergy (Oxford Instruments). The cross-sections of the films were prepared by a focused Ga-ion beam with energy of 30 kV. A Pt layer 1–2 μm in thickness was evaporated on the top of the sample to protect them from surface charging and destruction when preparing the cross-sections.

The samples were investigated using a Tecnai F20 (FEI) electron transmission microscope equipped with a field emission electron gun. The accelerating voltage was 200 kV. STEM images were acquired by a high angle annular dark field detector (HAADFD) from Fischione Instr.

Electrochemical measurements were carried out in a naturally aerated Hank's Balanced Salt Solution (HBSS) from Sigma-Aldrich Chemie GmbH, whose composition was as follows (g L^{-1}): 0.185 $CaCl_2 \times 2H_20$, 0.097 $MgSO_4$, 0.4 KCl, 0.06 KH_2PO_4, 0. 35 $NaHCO_3$, 8.0 NaCl, 0.048 Na_2HPO_4, 1.0 glucose and 0.011 Phenol

Red, pH 7.2–7.6. The measurements were performed at ambient temperature (20 ± 2°C). The polarization and EIS measurements were performed using a P/G/FRA system Parstat2273 (Princeton Applied Research). The Ag/AgCl electrode in a saturated KCl solution was used as a reference and the potentials referred to this electrode all through the paper. The counter electrode was a Pt plate of 4 cm^2. The working electrode was mounted in a special holder and placed into an electrochemical glass cell so that the area of the electrode exposed to the electrolyte was 0.5 cm^2.

The EIS spectra were measured at the open circuit potential (OCP) applying the perturbation of ±5 mV. The measurement frequency range was from 20 kHz to 0.1 Hz, this corresponded to a single scan of ~2 min. The ZSimpWin software was used for EIS data modelling.

RESULTS AND DISCUSSION

Figure 1 shows the XRD results obtained for Mg–Nb systems with different Nb content (4, 26 and 32 at.%). The XRD peaks indicate a crystalline structure of the deposits with the prevailing crystallite orientation <001>. The alloys with 4 and 26 at.% of Nb are substitutional solid solutions of Nb in the Mg lattice. At higher Nb concentrations, e.g. 32 at.%, the peaks characteristic of the niobium lattice are observed. Structural parameters of a solid solution depend on those of solute metal. Thus, the XRD peaks of Mg shift towards higher 2Θ values when Nb is introduced. This shift is caused by a decrease in the lattice parameters of Mg due to the partial substitution of larger Mg atoms by smaller Nb ones. The atomic radii of Mg and Nb are 0.15985 and 0.14318 nm, respectively [45]. A hexagonal closed packed (*hcp*) structure is characteristic of Mg and it is also retained for the alloys with the concentration up to ~26 at.% of Nb. The lattice parameter c_{Mg} of *hcp* structure decreased when introducing Nb: c_{Mg} = 5.211 Å was determined for an additive-free Mg, whereas this parameter decreased when Mg was introduced: $c_{Mg–4Nb}$ = 5.159 Å and $c_{Mg\text{-}26Nb}$ = 5.0769 Å. The contraction of the Mg lattice implies superior strength and hardness of Mg–Nb alloys when compared to those of pure magnesium. Introduction of Nb atoms into the Mg lattice also induces the grain-refinement effect. Average grain sizes of coatings were evaluated according to Scherrer's equation

$$D=\frac{0.94\lambda}{\beta\cos\Theta}, \quad (1)$$

where D is the grain size in nanometers, λ is the X-ray wavelength (λ = 0.154062 nm for CuK_α radiation), Θ is the diffraction angle of the peak. The parameter β stands for the line broadening at half the maximum intensity (FWHM) after subtracting

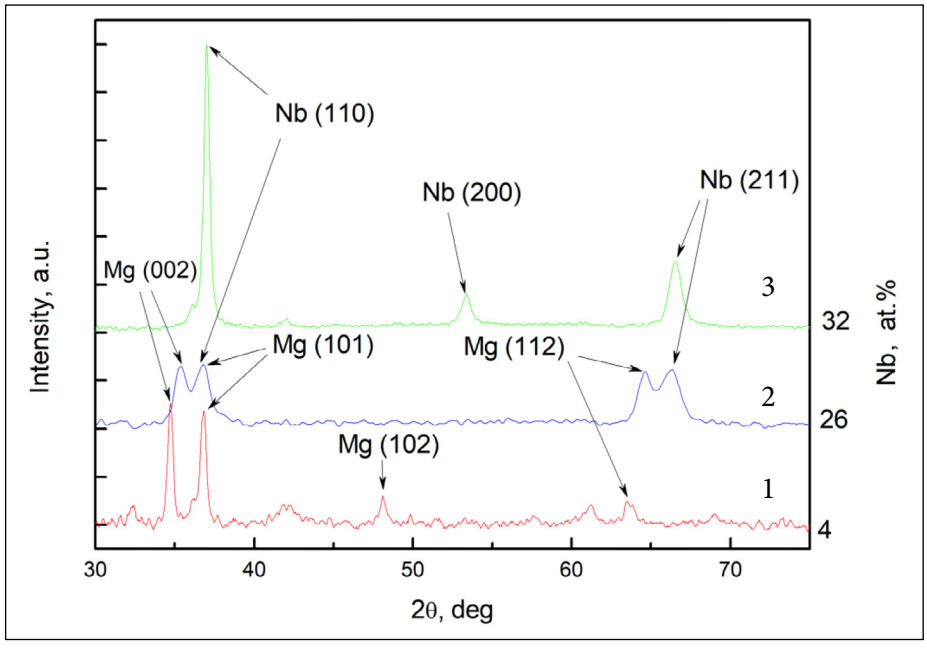

Fig. 1. XRD patterns of Mg–Nb alloys with different Nb content (at.%): 1 – 4, 2 – 26, 3 – 32

the instrumental line broadening. This parameter has been calculated as the difference $\beta = B - b$, where B is the integral width at FWHM for a sample and b is that for a standard (LaB_6, b = 0.016 rad). The β value was calculated according to the width of Mg 002 peak (Fig. 1). The alloys were found to be nanocrystalline with the grain sizes $D_{Mg\text{-}4Nb}$ = 90 nm and $D_{Mg\text{–}26Nb}$ = 25 nm.

At higher Nb concentration in the alloy (Mg–32Nb) a cubic body centred (*bcc*) structure is determined, which is typical of the Nb lattice (Fig. 1). Only minor quantity of the *bcc* phase was found for Mg–26Nb, whereas for Mg–32Nb alloy the *bcc* phase of Nb was completely prevailing.

Figures 2 to 4 show the STEM-HAADF images of the cross-sections of Mg–Nb films with different

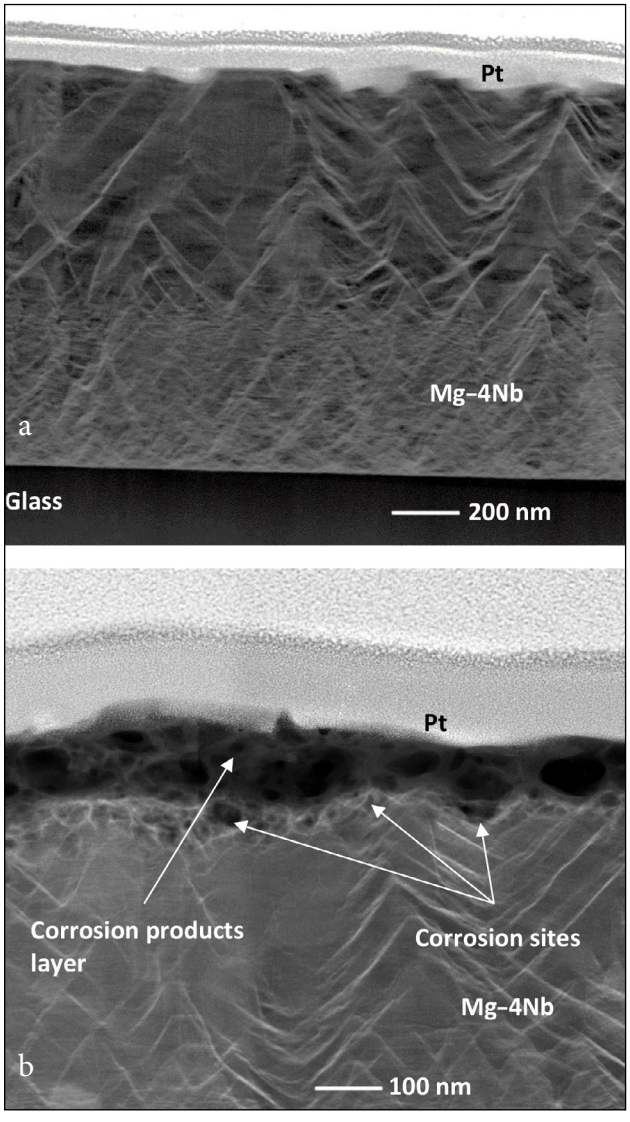

Fig. 2. STEM-HAADF images of the cross-section of Mg–4Nb alloy film. (a) as-deposited, (b) after ~5 min exposure in HBSS

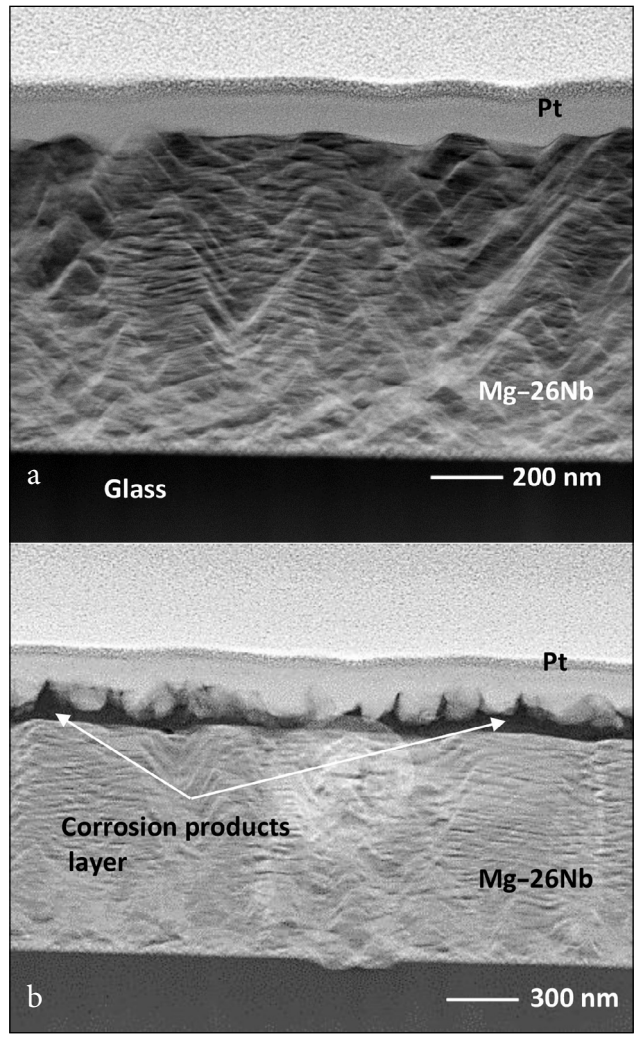

Fig. 3. STEM-HAADF images of the cross-section of Mg–26Nb alloy film. (a) as-deposited, (b) after ~5 min exposure in HBSS

Nb content. The images for the as deposited Mg–4Nb (Fig. 2) and Mg–26NB (Fig. 3) reveal a distinctive pyramid-like structure of the distribution of elements. At higher content of Nb, e.g. Mg–32Nb, no such structure is observed – distribution of both elements is homogeneous (Fig. 4). The HAADF registers the electron scattering power, which is proportional to the atomic weight of the sample constituents. The dark areas of the STEM image refer to a low signal density and identify the element of low atomic mass – ^{24}Mg. The light areas are attributable to the heavy element – ^{93}Nb. Thus, the dark-light areas map distribution of the elements within the Mg–Nb sample. The formation of the observed structure owes to a very low degree of affinity of both metals: Nb neither forms intermetallic phases with Mg nor dissolves in it [15, 16]. The MS deposition was performed at a partial pressure of Nb in the gas

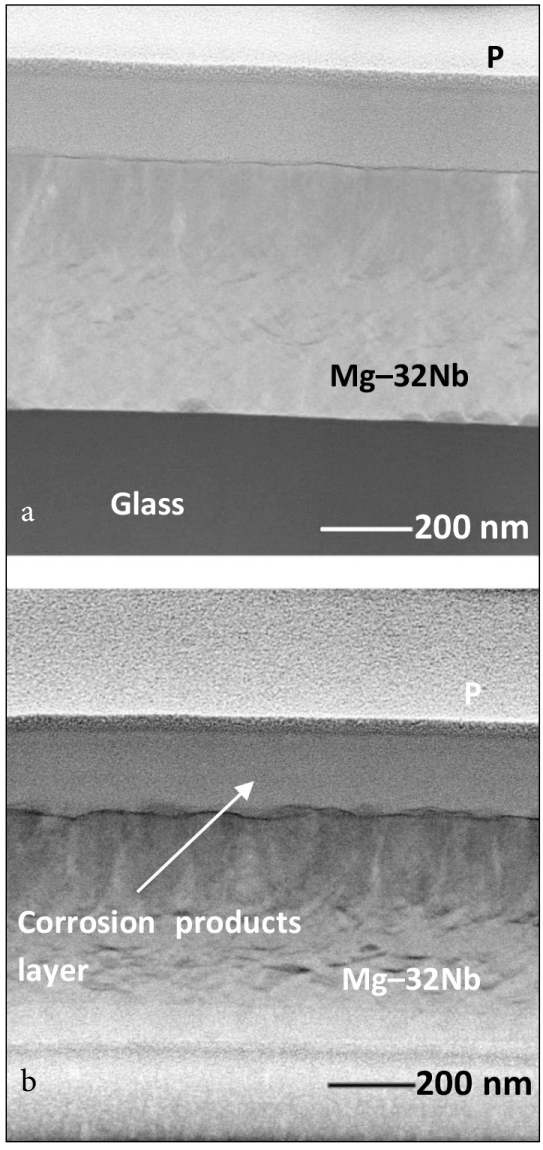

Fig. 4. STEM-HAADF images of the cross-section of Mg–32Nb alloy film. (a) as-deposited, (b) after ~5 min exposure in HBSS

phase much less than that of Mg ($p_{Nb,\,gas} << p_{Mg,\,gas}$). Thus, Mg deposition was prevailing at the beginning of MS so that some Mg-rich areas formed on the glass substrate. The Mg-rich phase grows up predominantly on the substrate by forming a specific cone- or pyramid-like structure. As a result, the adjacent gas phase depletes in Mg and the concentration ratio $p_{Nb,\,gas}/p_{Mg,\,gas}$ increases leading to prevalence of Nb deposition. Afterward, the situation changes to a vice versa one – the adjacent gas becomes enriched by Mg and depleted by Nb so that Mg depositions dominate again. There is no such Mg–Nb 'competition' when concentrations of the both components in the gas phase are similar, as it was true for the Mg–32Nb deposition (Fig. 4).

Corrosion of the produced alloys was studied by exposing them to HBSS. Magnesium is oxidized in the solution by water; some contribution could arise from the dissolved oxygen as well:

$$2H_2O + 2e^- \rightarrow H_2 + 2OH^- \ (E^0 = -0.828\ V_{H/H+}), \quad (2)$$

$$O_2 + 2H_2O + 4e^- \rightarrow 4OH^- \ (E^0 = 0.401\ V_{H/H+}), \quad (3)$$

$$Mg \rightarrow Mg^{2+} + 2e^- \ (E^0 = -2.372\ V_{H/H+}). \quad (4)$$

The reduction of dissolved oxygen (3) is typically neglected in Mg corrosion studies due to domination of water decomposition (2). In our case, both reactions should be taken into consideration. Due to a great difference between the standard potentials of O_2/OH– and Mg/Mg^{2+} couples, oxygen reduction should proceed under diffusion limitations. The upper limit of the current density of oxygen corrosion is estimated in stagnant (not stirred) solutions to be $j < 0.015$ mA cm^{-2} [46]. As will be shown below, the lowest corrosion rate under our conditions was of a similar value that is $j_{corr} = 0.016$ mA cm^{-2}. This means that contribution of (3) should not be excluded.

Both oxidation reactions (2) and (3) produce OH^- ions, which lead to a pH increase and precipitation of the corrosion products (e.g. magnesium hydroxide) on the corroding surface. The corrosion product layer is identified by HAADF on the corroded samples (Figs. 2b–4b), which originates from lower scattering power of the surface with ^{16}O and ^{1}H when compared to that of the metal phase. The data clearly show corrosion inhibition by Nb. About 100 nm surface layer develops on Mg–4Nb, whereas a much thinner layer (~10 nm) is observed on Mg–32Nb. The layer thickness on Mg–26Nb is around 50 nm, on average. This sample shows a specific layer morphology with distinctive peaks. Such non-uniform corrosion is inherited from the non-uniform distribution of Mg and Nb within the metallic phase, which may cause micro-galvanic effects. At lower c_{Nb} (Mg–4Nb), under analogous conditions, these effects were not detected, as development of the corrosion products is much more intensive and the layer spreads over a larger volume making the layer smoother.

Further corrosion features reveal the EIS data presented as the Nyquist plots at E_{ocp} (Fig. 5). Reliable data regarding the corrosion mechanism

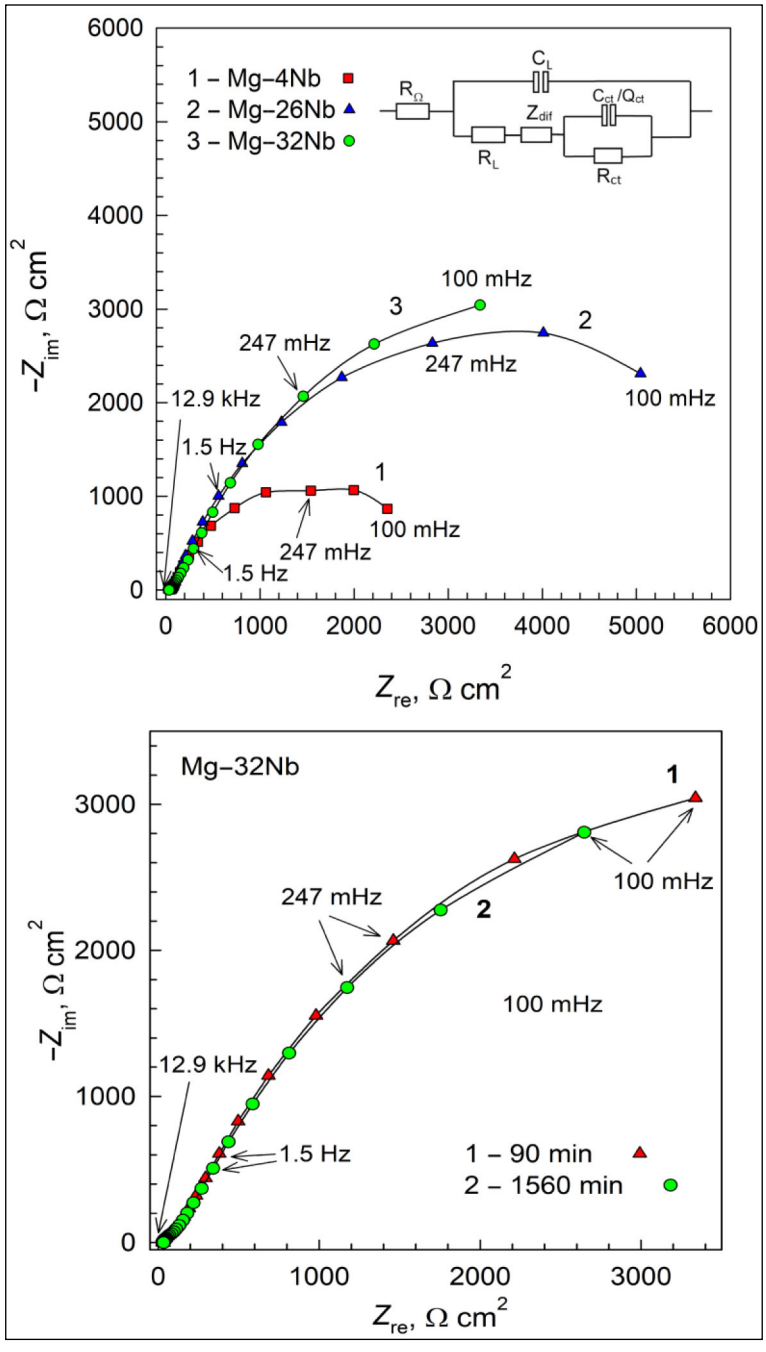

Fig. 5. Nyquist plots of Mg–4Nb (1), Mg–26Nb (2), Mg–32Nb (3) electrodes after 90 min of exposure to HBSS (upper chart). Lower chart compares the EIS data for the Mg–32Nb sample exposed to HBSS for 1.5 and 26 h. The inset shows EEC used for fitting of the EIS spectra: R_Ω is the resistance of the solution layer between the Luggin capillary and electrode, C_L is the capacitance of the porous layer, R_L is the electrolyte resistance and across the porous layer, Z_{dif} is the diffusion resistance across the porous layer, R_{ct} is $_{the}$ resistance of the charge transfer at the metal–solution interface at the bottom of the pore, and C_{ct}/Q_{ct} is the capacitance/constant phase element of the interface at the bottom

could be obtained when the electrode state does not change significantly during the EIS measurement. Otherwise, the spectrum will relate to a varying electrode state, which will compromise the data interpretation. The open circuit potential (E_{ocp}) shifts rapidly in the positive direction within 5–10 min after electrode immersion (Fig. 6). Then, the change becomes gradually suppressed and

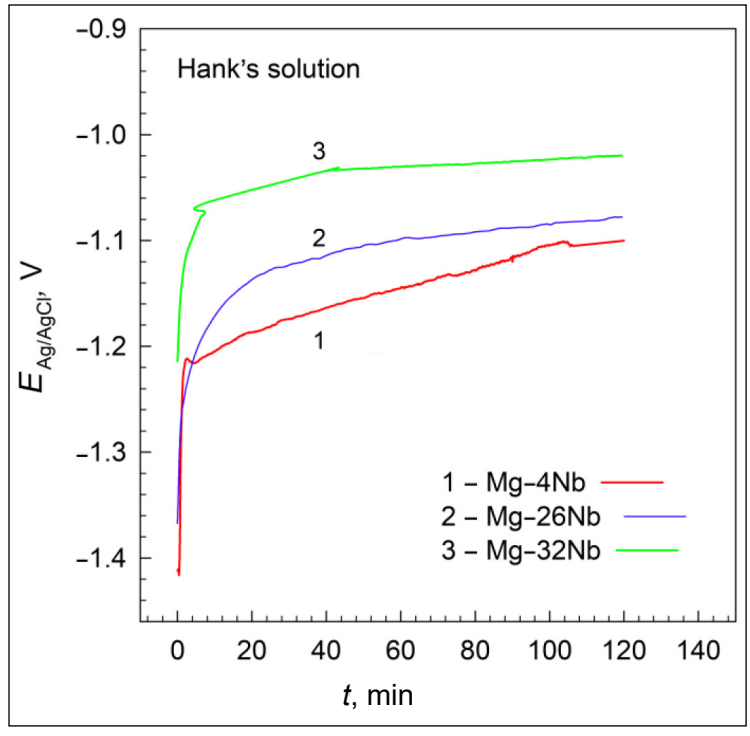

Fig. 6. E_{ocp} variation of Mg–4Nb (1), Mg–26Nb (2) and Mg–32Nb (3) electrodes in HBSS

a quasi-steady state is observed. This behaviour reflects the dynamics of the process (1)–(3): an active oxidation takes place at the first corrosion stages; the reactions are inhibited in the course of exposure owing to development of the passive layer. The EIS data in Fig. 5 refer to 90 min pre-exposure in the solution, at which according to E_{ocp} a quasi-steady state is achieved (Fig. 6).

The corrosion mechanism has been analysed by fitting the EIS data to the corresponding Equivalent Electric Circuit (EEC). This has been based on the minimization of the χ^2 function, defined as the sum of squares of the differences between the measured and calculated data. A validity of the fit was also controlled by assigning the acceptable value of the error of fitted parameters at <20% and the value of the impedance modulus error Z_{err} at <4–5%. Consistency of the EIS spectra with Kramers–Kronig transformation and the number of time constants (or RC-sub-circuits) that could be reliably resolved for each scan was assessed by the Measurement Model using the Voigt series [47, 48].

Satisfactory fitting was achieved when using the EEC as depicted in the inset of Fig. 7. This circuit models the impedance of the electrode covered with a porous passive layer, where the electrolyte resistance across the pore R_L is supplemented by the diffusion resistance Z_{dif}. Other elements included the capacitance of the solution-passive layer

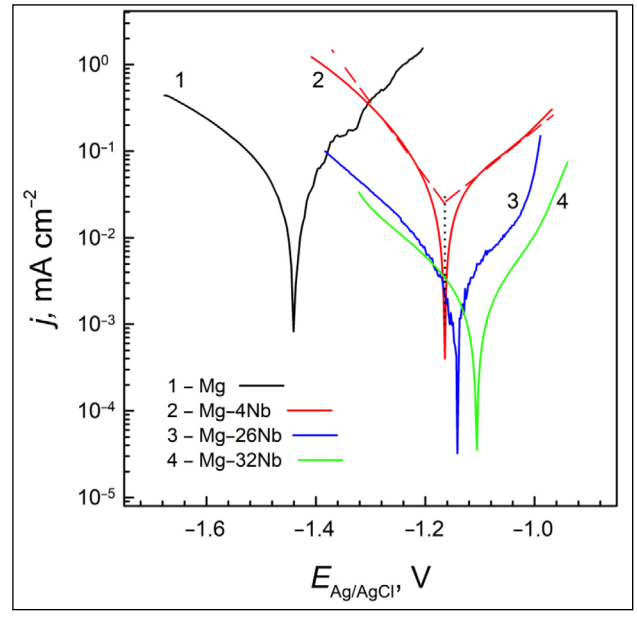

Fig. 7. Tafel plots of Mg (1) and Mg–Nb (2–4) electrodes in HBSS. Nb content (at.%): 1 – 0, 2 – 4, 3 – 26, 4 – 32. Immersion time prior to measurement was 5 min. The dotted line 2 shows subtraction of the ohmic potential drop. Tafel slopes: b_c (1 – 0.148, 2 – 0.116, 3 – 0.130, 4 – 0.130 V dec^{-1}), b_a (1 – 0.168, 2 – 0.198, 3 – 0.140, 4 – 0.140 V dec^{-1})

interface (C_L), the resistance of the solution layer between the Luggin capillary and electrode (R_Ω), the resistance of charge transfer at the metal–solution interface at the bottom of pores (R_{ct}) and the capacitance of this interface (C_{ct}). The derived parameters along with the values of χ^2 and Z_{err}, which characterize adequacy of the fitted spectra, are presented in the Table.

In general, there are different types of the diffusion element (Z_{dif}): Warburg (*W*), finite-space (*O*) and finite-length (*T*) elements as well as the Gerisher diffusion element (*G*) [49, 50]. The element *W* is used to model semi-infinite linear diffusion. The element *O* is the so-called porous bounded Warburg and *T* refers to the bounded Warburg. These elements model the process when a thin film and therefore finite diffusion are involved. They are characterized by two parameters: admittance Y_0 ($Y_0 = 1/Z$ at a given potential and $\omega = 1$ rad s^{-1} or $f \sim 0.16$ Hz) and time constant *B* (the time it takes for a reactant to diffuse through the film). The element *G* was firstly derived to account a chemical reaction that occurred in the solution bulk. Later on, Boukamp et al. applied this element to model diffusion within a porous electrode [51, 52]. The *G* element is characterized by Y_0 and a rate constant K_a. At high frequencies, the elements *O*, *T* and *G* are indistinguishable from the Warburg impedance. In our case, the best fitting was obtained when using the elements *G* (Mg–4Nb and Mg–24Nb) and *O* (Mg–32Nb) (Fig. 5 and Table).

The capacitance values C_L (Table) increase with c_{Nb} from $C_L = 1.1 \times 10^{-6}$ μF cm^{-2} for Mg–4Nb to $C_L = 8.6 \times 10^{-6}$ μF cm^{-2} for Mg–32Nb. The entire potential drop is determined by several contributions, i.e. those at the metal–oxide interface, within the oxide, in the Helmholtz layer and in the diffuse layer in the electrolyte. We do not discriminate, however, between these individual contributions assuming that C_L is affected mainly by the thickness of the corrosion product layer. The thickness of the corrosion product layer decreases with c_{Nb} about ten times (Figs. 2–4). Accordingly, C_L increases as it is in inverse proportion to the distance between the charged interfaces in the inner and outer parts of the corrosion product layer.

The EIS study reveals a high stability of the Mg–32Nb electrode over prolonged exposure in the solution. The spectrum recorded for this electrode after 1.5 h exposure did not differ greatly from the spectrum recorded after 26 h exposure (Fig. 5b) – only some minor reduction in both real and imaginary parts is observed during the prolonged exposure. To the contrary, high instability was exhibited by the Mg–26Nb electrode, whose Z_{re} decreased from ~5.1 to ~1.0 kΩ cm^2 during the same time of exposure. The analogous prolonged study for Mg–4Nb or pure magnesium was complicated due to high corrosion rates and dissolution (disintegration) of the film sample.

Quantitatively, the corrosion rate in electric units (j_{corr}, A cm^{-2}) could be obtained according to the classical Stern–Geary equation [53]

$$j_{corr} = \frac{b_c b_a}{2.3(b_c + b_a)R_p}, \quad (5)$$

where b_c and b_a are cathodic and anodic Tafel slopes, respectively, and R_p is the polarization resistance that is the voltammetric curve slope $R_p = \Delta E/\Delta j$ at E_{ocp}. In EIS measurements, R_p is obtained measuring the resistance at $\omega \to 0$. According to the applied modelling (Fig. 5), this resistance comprises several components connected in series:

Table. **Electrochemical parameters derived from the EIS data (Fig. 5) fitted according to the equivalent circuit shown in the figure**

Sample	R_0, Ω cm^2	C_L F, cm^{-2}	R_L, Ω cm^2	Z_{dif}	R_{ct}, Ω cm^2	C_{ct} or Q_{ct}, F cm^{-2}	χ^2 (Z_{err}, %)
Mg–4Nb	39	1.1×10^{-6}	13	G $Y_0 = 4.8 \times 10^{-4}$ $K_a = 3.6$	2348	29×10^{-5} $n = 0.98$	3.0×10^{-4} (<1.74)
Mg–26Nb	31	4.8×10^{-6}	11	G $Y_0 = 7.7 \times 10^{-4}$ $K_a = 5.19$	4970	14×10^{-5} $n = 0.93$	1.58×10^{-6} (<1.26)
Mg–32Nb	28	8.6×10^{-6}	16	O $Y_0 = 0.65 \times 10^{-4}$ $B = 1.16$	3115	41×10^{-5} $n = 0.99$	4.7×10^{-4} (<2.16)

$R_p = Z_{dif} + R_{ct} + R_L$. The Table shows that in our experiments only Z_{dif} and R_{ct} determine the R_p value, while R_L resistance is negligible. Thus, the corrosion rates could be calculated according to Eq. (5) using $R_p = Z_{dif} + R_{ct}$ derived from the EIS measurement (Table).

A discussion is necessary concerning the determination of Tafel slopes. A variety of factors influencing the Tafel behaviour of Mg-based electrodes was summarized by Bland et al. [54]. At rapid corrosion, such as in the case of pure Mg, errors are possible in the j_{corr} determination from Tafel plots due to such phenomena as change of the active area and the mechanism of the anodic corrosion reaction over the explored potential range. Kinetic parameters may vary depending on the exposure time, precipitation of corrosion products and surface pH. In addition, in the case of thin films, the anodic polarization time (e.g. potential sweep rate) becomes important, because the film could be disintegrated at prolonged polarization. Altogether, these factors could cause difficulties in data interpretation and, subsequently, errors in the determination of kinetic parameters, e.g. the corrosion rate. These difficulties, however, are of less importance in the case of corrosion resistant electrodes, as will be demonstrated in the case of Mg–32Nb.

The Tafel plots recorded at early stages of corrosion are given in Fig. 7. To determine precisely the Tafel slopes, it is necessary to account possible errors due to the substantial ohmic drop through the solution ($\Delta E_\Omega = jR_\Omega$). For instance, the plot for Mg–4Nb reaches the highest current density ~–1.0 mA cm^{-2} at the end of the cathodic curve and the EIS measurements identified the resistance R_Ω = 39 Ω cm^{-2} (Table). The ohmic subtraction at this point will be ΔE_Ω = 39 mV, which, when corrected, slightly decreases the slope: from 0.120 to 0.116 V dec^{-1} (dotted line 2 in Fig. 7). For other Mg–Nb curves, the analogous correction is negligible as the currents are much lower. The cathodic curves in Fig. 7 obey the Tafel law; extrapolation of them to E_{ocp} provides the corrosion current density. The slopes are in the range b_c ~ 0.116– 0.160 V dec^{-1}. Note that the slope value of cathodic hydrogen reduction (2) on an active electrode limited by a charge transfer is as high as b_c = 0.116 V dec^{-1} at T = 20°C [46]. The anodic curves exhibit a more complicated behaviour: they fail to exhibit a clear linearity region (curve 1 for Mg and 3 for Mg–24Nb). The anodic slope varies from b_a ~ 200 mV for Mg and Mg–4Nb to b_a ~ 130 mV for Mg–32Nb.

Qualitatively, the Tafel plots clearly indicate the inhibiting effect of Nb, which is evident from the positive E_{ocp} shift along with the shift down of the plots with c_{Nb}. One could conclude from the positive E_{ocp} shift that the inhibiting effect of Nb is more pronounced in respect to the anodic process (3).

One could expect that the errors in determination of kinetic parameters, due to a variety of the factors mentioned above, are less probable in the case of the electrodes of higher stability such as Mg–32Nb. Indeed, the corrosion rate of Mg–32Nb obtained from (5) was $j_{corr} = 1.6 \times 10^{-6}$ A cm^{-2} and this value was coincident with that obtained from the extrapolation of both cathodic and anodic Tafel plots. Great discrepancies were observed for actively corroding samples, for instance, the rate calculated for Mg–4Nb according to Eq. (5) was almost four times less than that obtained from the Tafel extrapolation: $j_{corr} = 2.7 \times 10^{-5}$ A cm^{-2} and $j_{corr} = 7.3 \times 10^{-6}$ A cm^{-2}, respectively.

The performed research shows that the applied electrochemical methods characterize well the qualitative features of Mg–Nb corrosion. These methods, however, have some limitations for quantitative assessment of the corrosion rate. The major difficulty appears at a rapid corrosion when determination of kinetic parameters is sensitive, first of all, to the surface factors such as precipitation of corrosion products, changes in the active surface area during exposure and polarization, as well as increase in surface pH. In this respect, gravimetric and analytical methods seem to be more reliable, however, these methods provide an integral information on the corrosion rate. Creation of new time-resolved methods of corrosion investigation is a challenge for the future research.

CONCLUSIONS

Mg–Nb alloy films having a thickness below 1 μm were deposited by magnetron sputtering on glass substrates with Nb concentrations of 4, 26 and 32 at.%. XRD identified nano-crystallinity of the deposits with grain sizes of the order of tens of nanometers.

STEM equipped with a HAADF detector identified fine Nb-enriched structures on a nanometer scale within the Mg μm Nb deposits.

The corrosion behaviour of the films has been studied in a balanced salt solution, whose pH and ion concentrations were close to those of the human blood plasma. EIS implied a localized corrosion with diffusion limitations within the corrosion products.

Voltammetry showed that Nb inhibited predominantly the anodic process that is Mg oxidation by water.

The corrosion rates were assessed in situ by Tafel extrapolation and the EIS-derived R_p method. Both methods provided reliable results on the corrosion rate of resistant alloy with ca. one third of Nb. At lower concentration, the assessment was equivocal.

Alloying of Mg with Nb makes it possible to adjust the corrosion activity of the alloy according to biomedical requirements for in vivo applications.

Received 18 May 2020
Accepted 27 May 2020

References

1. L. Kouisni, M. Azzi, M. Zertoubi, F. Dalard, S. Maximovitch, *Surf. Coat. Tech*., **185**, 58 (2004).
2. M. M. El-Omar, G. Dangas, I. Iakovou, R. Mehran, *Curr. Interv. Cardiol. Rep*., **3**, 296 (2001).
3. F. Feyerabend, J. Fischer, J. Holtz, et al., *Acta Biomater*., **6**, 1834 (2010).
4. G. Song, *Corr. Sci*., **49**, 1696 (2007).
5. A. C. Hanzi, P. Gunde, M. Schinhammer, P. J. Uggowitzer, *Acta Biomater*., **5**, 162 (2009).
6. M. Liu, P. Schmutz, P. J. Uggowitzer, G. Song, A. Atrens, *Corr. Sci*., **52**, 3687 (2010).
7. A. C. Hanzi, I. Gerber, M. Schinhammer, J. F. Löffler, P. J. Uggowitzer, *Acta Biomater*., **6**, 1824 (2010).
8. P. Gunde, A. C. Hänza, A. S. Sologubenko, P. J. Uggowitzer, *Mater. Sci. Eng*., **A528**, 1047 (2011).
9. T. Kraus, S. F. Fischerauer, A. C. Hanzi, P. J. Uggowitzer, J. F. Löffler, A. M. Weinberg, *Acta Biomater*., **8**, 1230 (2012).
10. H. Wang, Y. Estrin, Z. Zuberova, *Mater. Lett*., **62**, 2476 (2008).
11. Y. H. Yun, Z. Dong, D. Yang, et al., *Mat. Sci. Eng*., **C29**, 1814 (2009).
12. H. Hermawan, D. Dubé, D. Mantovani, *Acta Biomater*., **6**, 1693 (2010).
13. R. Godley, D. Starosvetsky, I. Gotman, *J. Mater. Sci.: Mater. Med*., **15**, 1073 (2004).
14. V. V. Starikov, S. L. Starikova, A. G. Mamalis, S. N. Lavrynenko, J. J. Ramsden, *J. Chem. Biol. Phys. Sci*., **7**, 141 (2007).
15. A. A. Nayeb-Hashemi, J. B. Clark, *Phase Diagrams of Binary Magnesium Alloys*, ASM International, Materials Park, OH (1988).
16. H. K. Westengen, in: K. H. Jurgen, R. W. Cahn, M. C. Flemings, B. Ilschner, E. J. Kramer, S. Mahajan (eds.), *Encyclopedia of Materials: Science and Technology*, p. 4739, Elsevier Science Ltd. (2001).
17. J. F. R. de Castro, S. F. Santos, A. L. M. Costa, A. R. Yavari, W. J. Botta F., T. T. Ishikawa, *J. Alloys Compd*., **376**, 251 (2004).
18. C. X. Shang, M. Bououdina, Z. X. Guo, *J. Alloys Compd*., **349**, 217 (2003).
19. S. Bao, Y. Yamada, K. Tajima, M. Okada, K. Yoshimura, *Jpn. J. Appl. Phys*., **46**, L13 (2007).
20. S. Bao, K. Tajima, Y. Yamada, P. Jin, M. Okada, K. Yoshimura, *Jpn. J. Cer. Soc*., **116**, 771 (2008).
21. P. Mengucci, G. Barucca, G. Majni, N. Bazzanella, R. Checchetto, A. Miotello, *J. Alloy Compd*., **509**, S572 (2011).
22. M. Shanthi, P. Jayaramanavar, V. Vyas, D. V. S. Seenivasan, M. Gupta, *J Alloy Compd*., **513**, 202 (2012).
23. B. Ham, X. Zhang, *Mat. Sci. Eng*., **A528**, 2028 (2011).
24. L. Toniutti, R. Checchetto, P. Mengucci, A. Miotello, R. S. Brusa, *Phys. Status Solidi C*, **6**, 2310 (2009).
25. K. Klyukin, M. G. Shelyapina, D. Fruchart, *Solid State Phenom*., **170**, 298 (2011).
26. V. Verdingovas, M. S. Jellesen, R. Ambat, *Microelectron. Reliab*., **73**, 158 (2017).
27. A. Banos, C. P. Jones, T. B. Scott, *Corros. Sci*., **131**, 147 (2018).
28. L. Staišiūnas, E. Juzeliūnas, K. Leinartas, et al., *Corrosion*, **75**, 1044 (2019).
29. J.-P. Wang, Y. Song, J.-K. Wang, et al., *Macromol. Mater. Eng*., **302**, 1700128 (2017).
30. A. M. Bazan, J. C. Galvez, E. Reyes, D. Gate-Lamuela, *Const. Build. Mater.*, **184**, 655 (2018).
31. R. A. De Motte, R. Barker, D. Burkle, S. M. Vargas, A. Neville, *Mat. Chem. Phys*., **216**, 102 (2018).
32. S.-Y. Cai, L. Wen, Y. Jin, *Int. J. Min. Met. Mater.*, **24**, 1112 (2017).
33. Y. Li, Y. F. Cheng, *Surf. Interface Anal.*, **49**, 133 (2017).
34. Y. Li, Y. F. Cheng, *Appl. Surf. Sci.*, **366**, 95 (2016).
35. C. Yu, P. Wang, X. Gao, *Science*, **10**, 6820 (2015).
36. F. Tang, Y. Chen, Z. Li, Y. Tang, G. Chen, *Const. Build. Mater.*, **175**, 14 (2018).
37. A. Potter, J. Sumner, N. J. Simms, *Mater. High Temp.*, **35**, 236 (2018).
38. S. Aouadi, N. Souissi, *Mater. Corros.*, **67**, 1105 (2016).
39. T. Kim, K. J. Choi, S. C. Yoo, Y. Lee, J. H. Kim, *Corros. Sci.*, **131**, 235 (2018).
40. C. Zhang, T. Zhang, Y. Wang, et al., *J. Electrochem. Soc.*, **162**, C754 (2015).
41. C. Luo, S. P. Albu, X. Zhou, et al., *J. Alloys Compd.*, **658**, 61 (2016).
42. A. B. Tesler, T. Sannomiya, A. Vaskevich, E. Saba, I. Rubinstein, *Adv. Optical Mater.*, 1800599 (2018).
43. M. Yasri, B. Lescop, E. Diler, F. Gallee, D. Thierry, S. Rioual, *Sens. Actuat. B*, **257**, 988 (2018).

44. E. Diler, F. Ledan, N. LeBozec, D. Thierry. *Mat. Corros.*, **68**, 1365 (2017).
45. *XRD Database 'Powder Diffraction File-2'* (integrated part of D8 Advanced Diffractometer software).
46. H. Kaesche, *Corrosion of Metals. Physicochemical Principles and Current Problems,* Springer, Berlin, Heidelberg, New York (2003).
47. P. Agarwal, M. E. Orazem, L. H. García-Rubio, *J. Electrochem. Soc.*, **139**, 1917 (1992).
48. M. Orazem, *J. Electroanal. Chem.*, **572**, 317 (2004).
49. M. Orazem, B. Tribollet, *Electrochemical Impedance Spectroscopy*, John Wiley & Sons, Inc., New Jersey (2008).
50. X. Z. Yuan, C. Song, H. Wang, J. Zhang, *Electrochemical Impedance Spectroscopy in PEM Fuel Cells. Fundamentals and Applications*, Springer-Verlag, London Lim (2010).
51. M. Gonzalez-Cuenca, W. Zipprich, B. A. Boukamp, G. Pudmich, F. Tietz, *Fuel Cells*, **1**, 256 (2001).
52. B. A. Boukamp, M. Verbraeken, D. H. A. Blank, P. Holtappels, *Solid State Ion.*, **177**, 2539 (2006).
53. M. Stern, A. L. Geary, *J. Electrochem. Soc.*, **104**, 56 (1957).
54. L. G. Bland, A. D. King, N. Birbilis, J. R. Scully, *Corrosion*, **71**, 128 (2015).

Konstantinas Leinartas, Eimutis Juzeliūnas, Laurynas Staišiūnas, Algirdas Selskis, Asta Griguceviči enė, Dalia Bučinskienė, Remigijus Juškėnas, Alma Ručinskienė

MG-NB LYDINIO KOROZIJOS BALANSINIAME DRUSKŲ TIRPALE PRADINIŲ STADIJŲ TYRIMAS STEM-HAADF IR EIS METODAIS

S a n t r a u k a

Plonos, mažesnio nei 1 μm storio, Mg-Nb lydinio dangos su Nb koncentracija 4, 26 ir 32 at.% buvo nusodintos magnetroniniu plazminiu būdu ant stiklo substratų. Elementų pasiskirstymas dangose buvo tirtas skenuojančiu peršviečiamu elektroniniu mikroskopu (STEM) su didelio kampo žiedinio tamsaus lauko detektoriumi (HAADF). Rentgeno spindulių difrakcijos metodu nustatyta lydinių nanokristalinė struktūra su kelių dešimčių nanometrų dydžio kristalitais. Dangų korozinė elgsena buvo tirta balansiniame druskų tirpale, kurio pH ir jonų koncentracijos yra artimos žmogaus kraujo plazmai. Elektrocheminės impedanso spektroskopijos (EIS) metodu nustatyta, kad vyksta lokali korozija su difuzijos apribojimais korozijos produktų sluoksnyje. *In situ* korozijos greičiai buvo nustatyti Tafelio ekstrapoliacijos metodu, o naudojant EIS metodą įvertintos poliarizacinės varžos. Korozijai atsparaus lydinio atveju, kurio sudėtyje yra apie trečdalis Nb, abiem metodais buvo nustatytos artimos, patikimos korozijos greičio vertės. Magnio legiravimas Nb suteikia galimybę kontroliuoti lydinių korozinį aktyvumą pagal biomedicininius reikalavimus, taikomus *in vivo*.